ACS SENSORS

pubs.acs.org/acssensors

Article

Cell Membrane and V_2C MXene-Based Electrochemical Immunosensor with Enhanced Antifouling Capability for Detection of CD44

Meiling Lian,* Yuqing Shi, Liuxing Chen, Yongji Qin, Wei Zhang, Jingbo Zhao, and Da Chen*

Cite This: *ACS Sens.* 2022, 7, 2701−2709

Read Online

ACCESS | Metrics & More | Article Recommendations | Supporting Information

ABSTRACT: The inactive adsorption and interference of biomolecules in electrochemical biosensors is a topic of intense interest. Directly utilizing native cell membranes to endow electrochemical surfaces with antifouling and biocompatible features is a promising strategy, rather than attempting to synthetically replicate complex biological interface properties. In this study, we present a facial and sensitive sandwich-type antifouling immunoassay through platelet membrane/Au nanoparticle/delaminated V_2C nanosheet (PM/AuNPs/d-V_2C)-modified electrode as the substrate of sensing interface and methylene blue/aminated metal organic framework (MB@NH_2-Fe-MOF-Zn) as an electrochemical signal probe. The biosensor perfectly integrates the high conductivity of AuNPs-loaded V_2C MXene with the excellent loading property of NH_2-Fe-MOF-Zn to improve the electrochemical sensing performance. In addition, the excellent antifouling properties of the homogeneous cell membrane can effectively prevent the non-specific adsorption of model proteins. The obtained antifouling biosensor possesses the capability of ultrasensitive detection of CD44 and CD44-positive cancer cell in complex liquids and exhibits good analytical performance for the analysis of CD44 with a linear range from 0.5 ng/mL to 500 ng/mL. This strategy of developing cell membrane-based biosensing systems with enhanced antifouling capability can be easily expanded to the construction of other complex biosensors, and the advanced biological probes and analytical methods provide a favorable means to accurately quantify biomarkers associated with tumor progression.

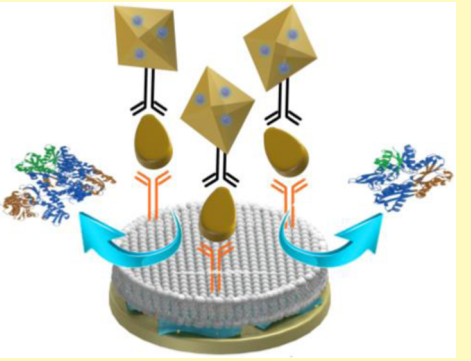

KEYWORDS: *electrochemical immunosensor, cell membrane, V_2C MXene, antifouling, CD44*

In the past few years, the electrochemical approach has become a widely used analytical technique for the detection of disease markers, taking intrinsic strengths of ultra-sensitivity, low cost, and high stability.[1−3] However, the biological interfaces face the persistent challenge of interference of biomolecules and inactive adsorption in complex backgrounds, specifically in the actual biological media.[4] This non-specific protein adsorption can reduce the diffusion of the target to the sensing interface, leading to decrease in performance of the sensor. To overcome these issues, the fabrication of an antifouling sensing interface by exploiting the properties of functional materials to prevent non-specific protein adsorption is an attractive strategy.[5,6] In recent years, a variety of antifouling materials, such as zwitterionic polymer,[7] polyethylene glycol (PEG),[8] and antifouling peptides,[9] have been widely used on electrochemical interfaces and show excellent selectivity in actual media. However, PEG and OEG are sensitive to oxidizing conditions, leading to unsatisfactory results for long-term applications.[10] Zwitterionic polymers, another major class of antifouling materials, are time consuming and complicated to synthesize.[11] In addition, most of the electrochemical platforms based on the above antifouling materials are used to detect whole blood, serum, and other substrates.[12] The platform used to detect cell expression will have validity and safety issues because these polymers either react with biomolecules or activate immune responses. Liu et al. developed an ultrathin cell-membrane-mimic film for tracking neurochemical dynamics in vivo. This coating not only maintains the electrode performance but also efficiently prevents protein adsorption.[13] Consequently, instead of trying to synthetically replicate the sophisticated biointerface characteristics, turning to nature for inspiration and obtaining design clues directly from biological systems will create new solutions.

Cell membranes play an important role in self-recognition, signal transduction, and biointerfacing.[14] The adoption of natural cell membrane coating is an emerging top-down technique that endows synthetic materials with various

Received: June 8, 2022
Accepted: August 23, 2022
Published: August 30, 2022

Scheme 1. Schematic Illustration of the Synthesis Procedure of d-V_2C MXene (a) as Well as MB@NH_2-Fe-MOF-Zn/Ab_2 (b) and the Fabrication Process of the Electrochemical Immunosensor with Antifouling Capability for Detection of CD44

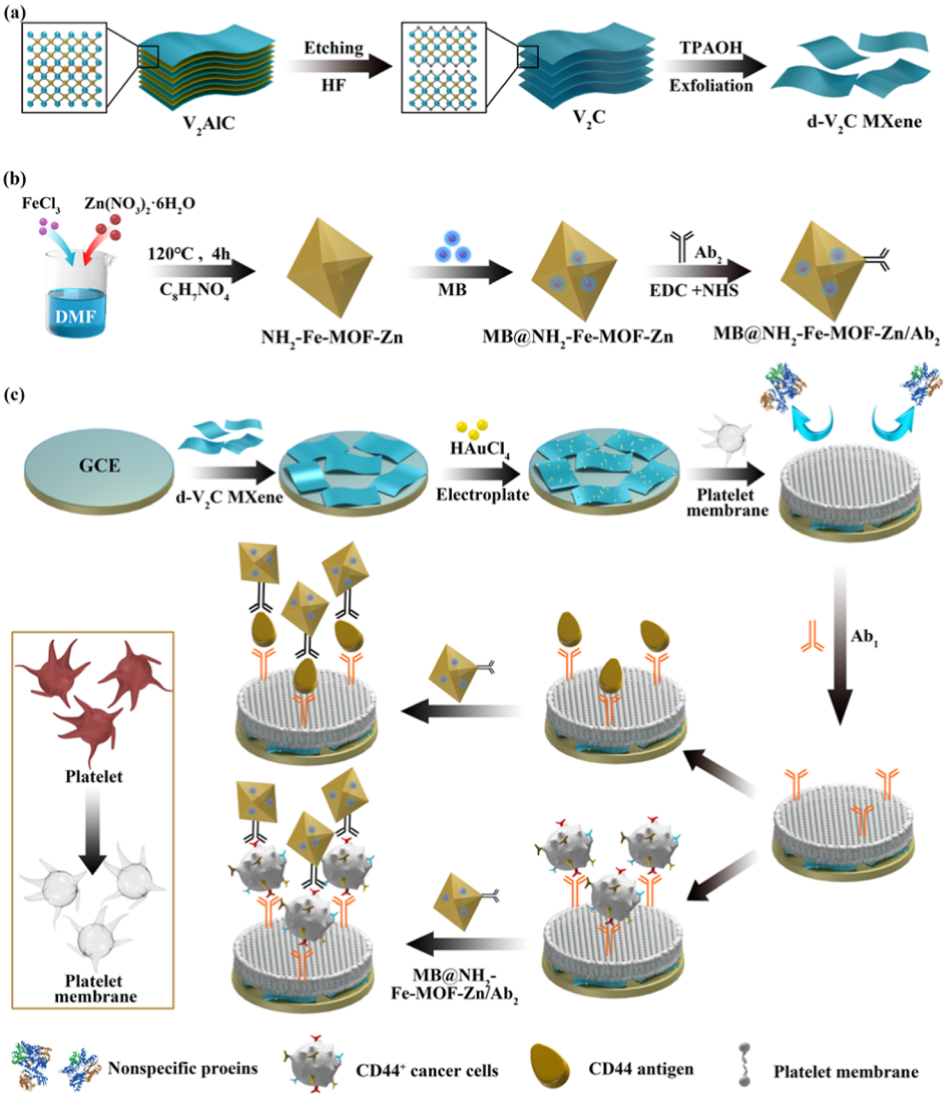

biological benefits and cell-like functions.[15] Based on this emerging approach, various cell membrane-derived materials inheriting desirable features were successfully created.[16,17] Meng et al. developed biomimetic particles by surface coating immunomagnetic micro/nanoparticles with red blood cell membranes.[18] This coating basically prevents the adsorption of proteins in the protein-riched plasma. Based on the design principle of natural platelet−cancer cell interaction, the human platelet membrane (PM) functionalized microchips were constructed for detecting cancer-derived extracellular vesicles in plasma samples.[19] Dong et al. fabricated a bioactive red blood cells membrane-based coating for orthopedic/dental implant, which presented excellent anti-biofouling capabilities.[20] Thus, using the fouling protection provided by the cell membranes, an electrochemical platform based on natural cell membranes may be able to effectively reduce non-specific biomolecule adsorption and provide a good biocompatibility interface for detecting cell expression. However, there are few reports on the application of PM functionalized detection interface in the assaying in complex media and construction of biosensors.

CD44, which is a family of cell adhesion molecules expressed on the surface of multiple cell types, participated in a variety of biological functions, such as cell proliferation, division, and migration.[21] The expression level of CD44 plays a key role in cancer metastasis and progression.[22] Compared with less-metastatic cells, CD44 is highly expressed in the migratory and metastatic tumor cells.[23] The level of CD44 on the surface of cancer cells is now used as a specific biomarker for the detection of malignant diseases.[24,25] Therefore, there is great need to develop effective strategies for CD44 detection and CD44-positive cancer cell identification without cell lysis.

Additionally, cell membranes are of poor conductivity, which greatly limits their application in electrochemical biosensors, especially for tumor marker detection. Introducing a new material and a novel strategy would be an alternative to this problem. MXenes, a family of two-dimensional (2D) nanomaterials, have revealed beneficial applications in catalysis, sensing, and biotechnology due to their unique structural properties as well as remarkable thermal, electrical, and mechanical properties.[26−28] However, the MXene-based electrochemical sensors were focused on Ti_3C_2,[29−31] while little investment was there in V_2C exploration.

https://doi.org/10.1021/acssensors.2c01215
ACS Sens. 2022, 7, 2701−2709

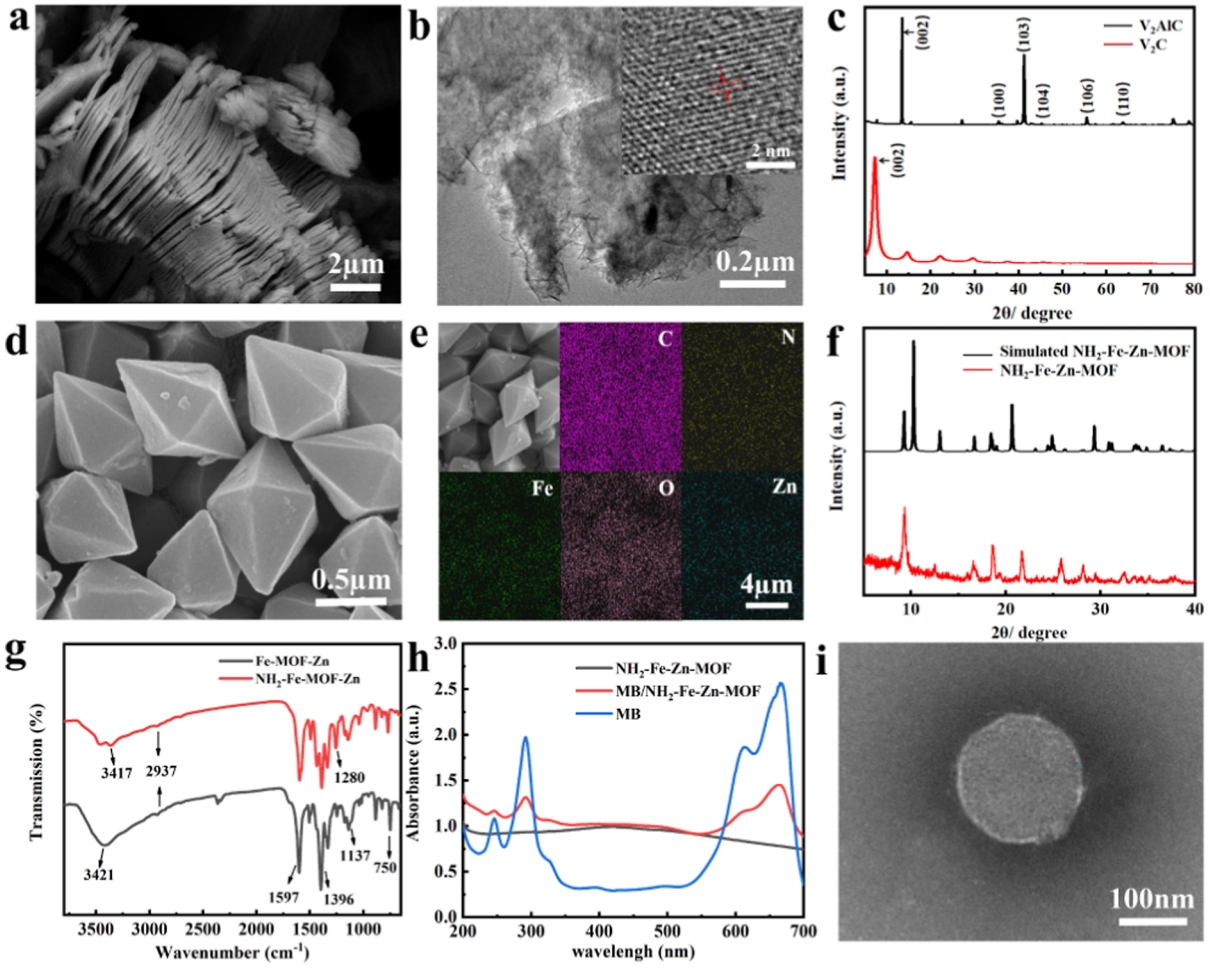

Figure 1. (a) SEM image of the V_2C nanosheets. (b) TEM image of the d-V_2C nanosheets (inset: HRTEM images of d-V_2C). (c) XRD patterns of V_2AlC nanosheets and d-V_2C nanosheets. (d) SEM image of NH_2-Fe-MOF-Zn and the elemental mapping in NH_2-Fe-MOF-Zn (e). (f) XRD patterns of NH_2-Fe-MOF-Zn. (g) FT-IR spectra of Fe-MOF-Zn and NH_2-Fe-MOF-Zn. (h) UV−visible absorption spectrum of MB, NH_2-Fe-MOF-Zn, and MB@NH_2-Fe-MOF-Zn. (i) TEM image of the PM.

In view of this, a sandwich-type electrochemical antifouling immunosensor with PM/Au nanoparticle/delaminated V_2C nanosheet (PM/AuNPs/d-V_2C)-modified electrode as a platform and methylene blue/aminated metal organic framework (MB@NH_2-Fe-MOF-Zn) as a signal indicator for accurate detection of CD44 was fabricated in this work (as shown in Scheme 1). The electrode was first modified with d-V_2C, and AuNPs were then in situ electrodeposited on the electrode surface to improve the electrochemical conductivity. PM and anti-CD44 Ab (Ab_1) were further modified on the AuNPs/d-V_2C interface to block the non-specific adsorption and capture the CD44 selectively. Moreover, the modified Fe-MOF-Zn containing sufficient amine groups enhanced the load capacity of MB and the covalent binding of anti-CD44 Ab (Ab_2). Once specific recognition occurred between antibody and antibodies, the quantitative detection of CD44 was realized by observing the increase in differential pulse voltammetry (DPV) signal from MB. The as-proposed immunosensor was applied to the identification of CD44-positive cancer cells and the determination of target protein CD44 with satisfactory results. This electrochemical system with excellent antifouling ability and biocompatibility holds great promise for directly analyzing cells and determining tumor cell types.

EXPERIMENTAL SECTION

Materials and Reagents. Citric acid, uric acid (UA), glucose (Glu), chloroauric acid ($HAuCl_4$), sodium hydrogen phosphate (Na_2HPO_4), potassium ferrocyanide ($K_4[Fe(CN)_6]$), and potassium ferricyanide ($K_3[Fe(CN)_6]$) were obtained from Zhengzhou Acme Chemical Co., Ltd. Ferric trichloride ($FeCl_3$), zinc nitrate ($Zn(NO_3)_2$), amino terephthalic acid, 1-hydroxy-2,5-pyrrolidine dione (EDC), and *N*′-(ethyleneimine methylenediamine)-*N*,*N*-dimethyl-1,3-propylene diamine monohydrochloride (NHS) were purchased from Shanghai Aladdin Biochemical Technology Co., Ltd. Methylene blue (MB) was bought from J&K Scientific Co., Ltd. FITC-labeled BSA and CD44 human monoclonal antibody were purchased from Beijing Solarbio Science & Technology Co., Ltd. Anticoagulation cattle blood was purchased from Guangzhou Hongquan Biology Co., Ltd. MDA-MB-231 cancer cells and MCF-7 cancer cells were obtained from the Chinese Academy of Sciences (Beijing bena culture collection) and maintained in Eagle (Sigma) medium with 10% fetal bovine serum (FBS) in a humidified 5% CO_2 incubator at 37 °C. To harvest cells, 1 mL of trypsin (0.25% by V/V) was dropped into the cell culture flask for 4 min in the CO_2 incubator. Finally, obtained cells were washed three times with phosphate-buffered saline (PBS) (pH = 7.0, 0.1 M) buffer for sensing.

Apparatus. Scanning electronic microscopy (SEM) images and energy-dispersive spectrometer (EDS) mapping were captured using a Quanta 250 FEG SEM. Fourier transform infrared (FT-IR) measurement was obtained by Bruker Tensor 27 FT-IR with DTGS detector. X-ray photoelectron spectroscopy (XPS) spectra were

https://doi.org/10.1021/acssensors.2c01215
ACS Sens. 2022, 7, 2701−2709

obtained from a Kratos AXIS SUPRA spectrometer. X-ray diffraction (XRD) pattern was observed by an Ultima IV system equipped with Cu Kα radiation. The electrochemical experiments were carried out on an LK5100 electrochemical luminescence analysis system with a three-electrode system. The glassy carbon electrode (GCE) (diameter = 3 mm) was used as the working electrode, and platinum wire and Ag/AgCl were used as auxiliary and reference electrodes, respectively.

Preparation of d-V_2C. V_2AlC was added to the HF solution (50%), and the reaction was carried out at 55 °C under magnetic stirring for 72 h. The above corrosion product was then washed continuously with deionized water until the pH of the supernatant was 7.0. Then, the product was dried in a vacuum oven at 60 °C for 12 h to obtain multilayer V_2C nanosheets. The above corrosion products (1 g) were added to tetrabutylammonium hydroxide (10 mL), stirred for 24 h, and centrifuged for 1 h at 4000 rpm to obtain the stable colloidal suspension of delaminated V_2C nanosheets (d-V_2C).

Preparation of MB@NH_2-Fe-MOF-Zn/Ab_2. $FeCl_3$ (146 mg), $Zn(NO_3)_2{\cdot}6H_2O$ (30 mg), and 2-amino terephthalic acid (181 mg) were added to DMF (50 mL), stirred for 10 min, and then reacted at 120 °C for 4 h. When the temperature dropped to room temperature, NH_2-Fe-Zn-MOF nanomaterials were obtained by centrifugation for 5 min at 8000 rpm. After centrifugation and washing once with DMF and anhydride ethanol, it was dried in a vacuum oven (60 °C, 12 h). The above product (10 mg) and MB (25 mg) were added to deionized water (5 mL) and reacted for 8 h under magnetic stirring at a speed of 800 rpm at 4 °C. After washing with DMF and absolute ethanol for 4 times, it was dried in a vacuum oven (60 °C, 6 h) to obtain a blue solid MB@NH_2-Fe-MOF-Zn composite material. The prepared material was added to 0.5 mL 2 mM NHS and 0.5 mL 10 mM EDC (prepared with PBS solution at pH = 7.0), followed by CD44-Ab_2 (1 mL, 10 μg/mL) solution. The mixed solution was stirred slightly at 4 °C for 12 h to obtain MB@NH_2-Fe-MOF-Zn/Ab_2 mixed solution.

Preparation of Platelet Membrane. Bovine whole blood (10 mL) was centrifugated for 5 min at a speed of 1780 rpm. Then, the supernatant was centrifugated at a speed of 4590 rpm for 5 min to obtain precipitation. The precipitates were suspended in water and stored at −80 °C for 5 h. The platelet suspension was removed from the −80 °C environment and thawed at room temperature. After thawing, it was centrifuged for 4 min at 12980 rpm. The precipitates were resuspended in deionized water and stored at −80 °C for 5 h. And the PM suspension could be obtained after repeated freezing and thawing for three times.

Preparation of Immunosensors. Dropping of d-V_2C (6 μL) on a clean GCE and d-V_2C-modified GCE was developed (d-V_2C/GCE). d-V_2C/GCE was placed in an electrolytic tank containing $HAuCl_4$ (5 mL, 0.2 M), and the scanning potential was −0.9−0.3 V for 10 cycles by cyclic voltammetry (CV) and dried to obtain the AuNPs/d-V_2C/GCE. The prepared PM suspension (5 μL) was taken and dropped on the electrode surface and incubated at 37 °C for 1 h. Then, the CD44-Ab_1 (5 μL, 10 μg/mL) solution was added and incubated at 4 °C for 12 h to obtain Ab_1/PM/AuNPs/d-V_2C/GCE. After washing with 0.1 M PBS, different concentrations of CD44 solution or MD-MBA-231 cells/MCF-7 cells (prepared with PBS solution with pH = 7.0) were incubated on the electrode surface at 37 °C for 1 h. Finally, after washing with 0.1 M PBS, the prepared MB@NH_2-Fe-MOF-Zn/Ab_2 was dropped onto the electrode surface and incubated at 37 °C to obtain MB@NH_2-Fe-MOF-Zn/Ab_2/CD44/Ab_1/PM/AuNPs/d-V_2C/GCE. DPV measurements were carried out in the range of −0.6 to 0.1 V with an amplitude of 50 mV and a pulse width of 0.05 s. CV responses were recorded in the range of −0.3 to 0.8 V.

RESULTS AND DISCUSSION

Characterization of d-V_2C and NH_2-Fe-MOF-Zn. Two-dimensional V_2C was prepared by selectively HF-etching the Al layers from V_2AlC.[32] Then, the 2D V_2C nanosheets were intercalated in a tetrapropylammonium hydroxide (TPAOH) solution to exfoliate them into delaminated V_2C nanosheets (d-V_2C). The morphology of the V_2C nanosheets and d-V_2C nanosheets was measured by SEM and transmission electron microscopy (TEM). Figure 1a,b shows that the obtained V_2C nanosheets present accordion-like layered stacks, while d-V_2C exhibits a monolayer sheet morphology. Moreover, it can be clearly seen from high-resolution transmission electron microscopy (HRTEM) images (the inset in the Figure 1b) that d-V_2C are highly oriented along the (002) crystal plane and the estimated interplanar distance is about 0.97 nm. Then, XRD patterns were used to characterize the crystal structure of V_2AlC nanosheets and as-synthesized V_2C nanosheets (Figure 1c). Several peaks at V_2AlC nanosheets appear on the crystal surfaces of (100), (002), (103), (104), (110), and (106), which are consistent with the previous reports.[33] After the etching of V_2AlC, the characteristic diffraction peak with 2θ about 8° can be assigned to the (002) plane of d-V_2C, confirming the formation of d-V_2C.[34] XPS measurements were further executed to explore the valence states of V_2C. Figure S1 displays XPS wide-range spectra of d-V_2C with high-resolution spectra of V 2p and C 1s. The wide spectrum of d-V_2C shows that the sample after HF treatment is mainly composed of V, O, C, and F elements and contains surface groups −F, −O, and so forth (Figure S1a). In the XPS spectrum of V 2p, the peaks at 517.1 and 524.4 eV originate from the V−C bond and V−O bond. The binding energies of O^{2-} and O−H bonds are 530.3 and 531.3 eV, respectively, which may be caused by the presence of oxygen-containing functional groups formed after HF etching and water produced during the purification process. In the XPS spectra of C 1s, the peaks at 283.2 and 286.6 eV are attributed to the V−C bond, and the binding energies of the C−C bond and O−C═O bond are 284.8 and 288.9 eV, respectively.[35] The C−O bond may be derived from the oxidation of d-V_2C, and the C−C bond may be formed by the selective termination of V during surface carbon deposition and/or etching.

SEM obtained detailed information on the surface morphology and was used to investigate the characterization of NH_2-Fe-MOF-Zn. As shown in Figure 1d, it is observed in the SEM image that NH_2-Fe-MOF-Zn exhibits chiral octahedral morphology, and its diagonal length is about 1200 nm. Small particles on the surface of NH_2-Fe-MOF-Zn may be caused by impurities formed from raw material residues during material synthesis. The corresponding EDS spectra showing the C, N, Fe, O, and Zn elements presented in the MOF can clearly be observed (Figure 1e). The XRD pattern shows that the information of NH_2-Fe-MOF-Zn is similar to the simulated MIL-88, suggesting that NH_2-Fe-MOF-Zn was successfully synthesized (Figure 1f). It is worth noting that the XRD spectrum does not completely match the peak of the simulated model of MIL-88. The discrepancy in relative intensity may be due to a result of a difference in synthetic methods. The surface survey XPS analysis of NH_2-Fe-MOF-Zn is displayed in Figure S2. The results show the existence of C, O, N, Fe, and Zn elements, which means the successful preparation of the material. The spectrum of C 1s is deconvoluted into two prominent bands centered at C−N (285.8 eV) and C−C (281.8 eV). The spectrum of O 1s can also be analyzed into two peaks at C═O (529 eV) and Fe-O/Zn-O (430 eV). The N 1s XPS spectrum shows that there are three binding modes of N, pyrrole nitrogen (N-5) at 396 eV, pyridine nitrogen (N-6) at 397.7 eV, and $-NH_x$ at 403.5 eV, indicating that $-NH_2$ exists in the surface of electroactive NH_2-Fe-MOF-Zn. The Fe 2p XPS spectrum can be divided into three peaks that appear

https://doi.org/10.1021/acssensors.2c01215
ACS Sens. 2022, 7, 2701−2709

at 708.9, 714, and 723.5 eV, which can be assigned to Fe $2p_{2/1}$, satellite peak, and Fe $2p_{3/2}$, respectively.[36] The Zn 2p XPS spectrum is fitted into two peaks; the peaks occur at 1045.5 and 1018.9 eV that are consistent with Zn $2p_{2/1}$ and Zn $2p_{3/2}$.

The functional groups in sample structures were characterized using FT-IR spectroscopy. Compared to Fe-MOF-Zn, NH_2-Fe-MOF-Zn has three additional peaks in the FT-IR characterization (Figure 1g). The one located at 1280 cm^{-1} is attributed to the C−N vibration of the amino group on the benzene ring, and the two at 3417 and 2937 cm^{-1} originate from the stretching of ν_s (N−H) and ν_{as} (N−H).[37] The FT-IR spectrum confirms that the NH_2-Fe-MOF-Zn was indeed modified by amino groups. The functionalized NH_2-Fe-MOF-Zn provides more sites for the loading of MB as an electrochemical signal probe and the connection of CD44 antibody molecules. UV spectrophotometry was carried out to verify the successful loading of MB in NH_2-Fe-MOF-Zn. In Figure 1h, MB loaded in the NH_2-Fe-MOF-Zn gave rise to a characteristic absorption peak at 246, 292, 613, and 665 nm, which was comparable to that observed for MB. The above-mentioned results explained the successful synthesis of MB@NH_2-Fe-MOF-Zn. PM was prepared from platelet-rich plasma using the protocol previously described.[38] The TEM image of PM reveals a characteristic core−shell structure (Figure 1i). The size distribution and surface charge (Figure S3) are also consistent with previous reports, demonstrating the successful synthesis of PM.[19]

Investigation of the Antifouling Performances. The hydrophilic surface can reduce the adsorption of non-specific proteins, which is the key to constructing an antifouling surface. Therefore, the water contact angles of electrodes modified with different materials are explored. As shown in Figure 2a, the contact angle of bare GCE was 64.35°, which

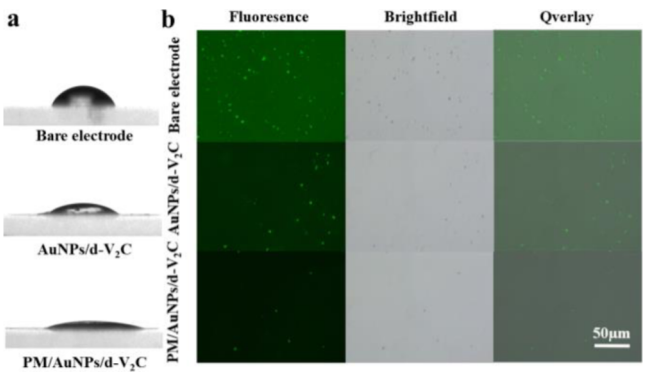

Figure 2. (a) Contact angle images of bare electrode, AuNPs/d-V_2C, and PM/AuNPs/d-V_2C. (b) Laser confocal imaging of the bare electrode, AuNPs/d-V_2C, and PM/AuNPs/d-V_2C-modified electrodes after soaking in FITC-labeled BSA (0.2 mg/mL) for 30 min.

decreased to 37.35° and 16.62° after modification with AuNPs/d-V_2C and PM, respectively. The above results indicate that the PM-modified electrode surface has good hydrophilicity and potential to construct an antifouling sensing interface. The wettability is also an important parameter to improve the biocompatibility of materials, so the PM-modified interface can improve the biocompatibility of the electrode to improve the sensor performance.

The antifouling ability of intuitive characterization was further performed with confocal laser imaging. It can be seen from Figure 2b that a large amount of FITC-BSA is adsorbed on the bare GCE surface and AuNPs/d-V_2C-coated electrode, indicating that there is serious non-specific protein adsorption (FITC-labeled BSA). After similar treatment with FITC-labeled BSA, no obvious fluorescence is seen on the PM-modified surface. These results further indicated that the PM-modified interface displayed excellent protein rejection ability. The antibacterial fouling ability of PM coating mainly depends on the steric hindrance of glycoproteins and the abundance of zwitterionic headgroups in phospholipid bilayers[20] as well as the good hydrophilicity of the interface.

Then, the antifouling properties of the PM/AuNPs/d-V_2C-modified electrode was evaluated using the DPV method in 5 mM $[Fe(CN)6]^{3-/4-}$ containing 0.1 M KCl. As shown in Figure 3a,b, the significant current changes of the bare GCE and AuNPs/d-V_2C/GCE were observed after soaking in various concentrations of FBS samples for 30 min. As expected, the current of the PM/AuNPs/d-V_2C-modified biosensor changes very slightly (Figure 3c). After incubation with 100% FBS, the DPV signal of the bare GCE and AuNPs/d-V_2C modified biosensor is reduced by 46.75 and 27.38%, respectively. Moreover, the PM-modified biosensor surface just slightly decreased by 7.87%, retaining most of the original signal (Figure 3d). These results clearly proved that the PM-modified electrode surfaces have effective anti-non-specific adsorption properties.

Characterization of Immunosensor. To investigate the step-wise fabrication process of the modified electrode, CV measurements were well recorded to detect the electrochemical behaviors of different immunosensors in 5 mM $[Fe(CN)6]^{3-/4-}$ (as a redox probe). As shown in Figure 4a, GCE (curve i) exhibits a pair of well-defined redox peaks. After modification of d-V_2C (curve ii) and AuNPs (curve iii), the peak current was obviously increased, attributing to the excellent electrical conductivity of d-V_2C and AuNPs. Subsequently, by the addition of PM to prevent the non-specific bindings, the redox current decreased markedly (curve iv). When Ab_1 (curve v), CD44 as a target (curve vi), and MB@NH_2-Fe-MOF-Zn/Ab_2 (curve vii) as the tracer were modified, the peak redox current was decreased successively. This can be ascribed to the hindered electron transfer and mass transfer between the electrode surface and active material due to the gradual introduction of protein molecules. Overall, these changes in the current can indicate the successful formation of immunocomplex.

EIS is an effective strategy for monitoring changes in surface characteristics of electrochemical immunosensors. Thus, the EIS characterization was employed to further confirm the CV results. Figure 4b shows the impedance spectra of electrodes with different modification processes, from which it can be seen that each impedance spectrum includes two parts. Generally speaking, the diameter of the semicircle in the high-frequency region of the Nyquist impedance curve is equal to the value of the electron transfer resistance (R_{et}), which is affected by the electron transfer process. After modification of d-V_2C on the bare GCE (curve i), d-V_2C/GCE exhibited a small R_{et} value (curve ii) owing to its certain conductivity. The electrodeposition of AuNPs leads to a further decrease in the R_{et} value of the AuNPs/d-V_2C/GCE (curve iii). By successfully immobilizing the PM on the electrode surface, the surface resistance was significantly increased (curve iv). When PM/AuNPs/d-V_2C/GCE was modified with Ab_1 (curve v), CD44 (curve vi), and MB/NH_2-Fe-MOF-Zn/Ab_2 (curve vii), the R_{et} value was remarkably increased, which was

https://doi.org/10.1021/acssensors.2c01215
ACS Sens. 2022, 7, 2701−2709

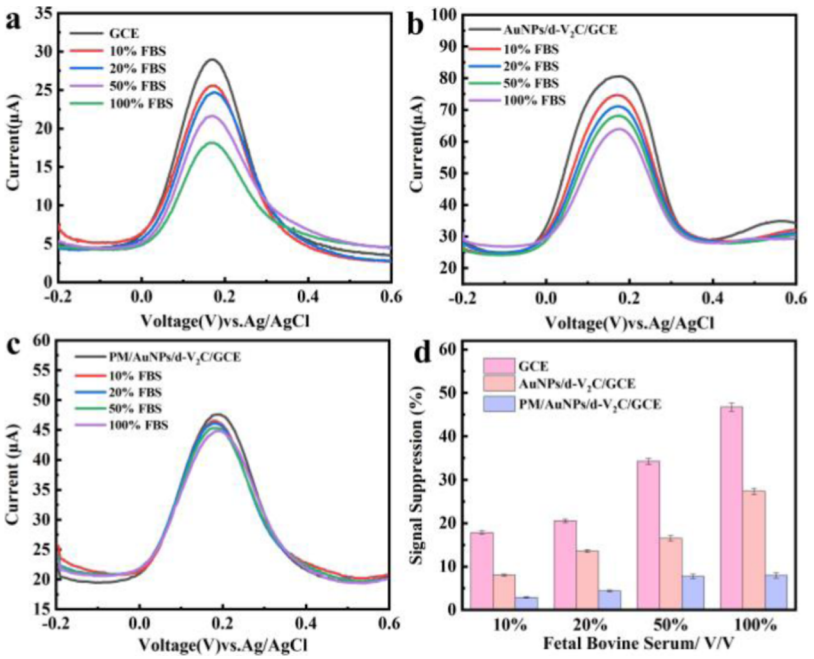

Figure 3. (a) DPV responses of biosensor with (a) GCE, (b) AuNPs/d-V_2C/GCE, and (c) PM/AuNPs/d-V_2C/GCE in 5 mM $[Fe(CN)_6]^{3-/4-}$ containing 0.1 M KCl after incubation in different concentrations of FBS samples. (d) Antifouling performance analysis histogram of biosensor with GCE, AuNPs/d-V_2C/GCE, and PM/AuNPs/d-V_2C/GCE based on the electrochemical signal.

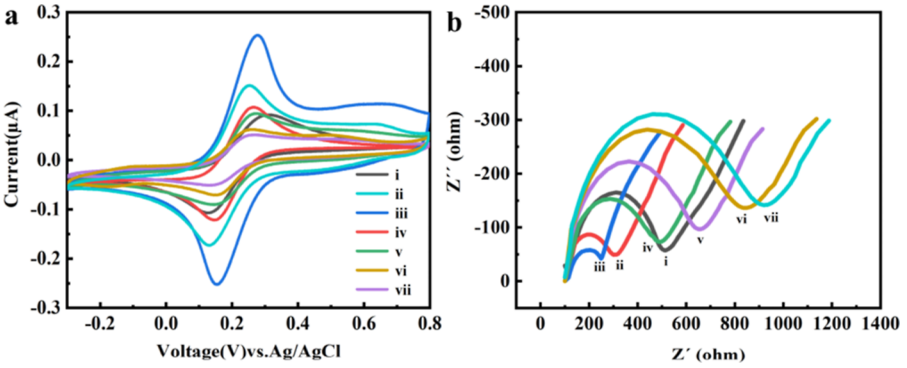

Figure 4. (a) Cyclic voltammograms and (b) EIS response (frequency range: 100000−0.1 Hz, wave amplitude: 15 mV) at (i) bare GCE, (ii) d-V_2C/GCE, (iii) AuNPs/d-V_2C/GCE, (iv) PM/AuNPs/d-V_2C/GCE, (v) Ab_1/PM/AuNPs/d-V_2C/GCE, (vi) CD44/Ab_1/PM/AuNPs/d-V_2C/GCE, (vii) MB@NH_2-Fe-MOF-Zn/Ab_2/CD44/Ab_1/PM/AuNPs/d-V_2C/GCE. The measurements were carried out in 5.0 mM $[Fe(CN)_6]^{3/4-}$ containing 0.1 M KCl.

attributed to the shielding effect of the immunocomplexes (antibody-antigen) on the electrode surface. The above results are consistent with the changes in the electron transfer observed by CV. In addition, it can be seen from Figure S4 that the delaminated V_2C has a smaller resistance than the multilayer V_2C, which means that the delaminated V_2C has better conductivity and can accelerate the electron transfer rate at the interface.

Optimization of Conditions for Immunosensor. For optimal analytical performance on CD44, the conditions of the experiment including the pH, the concentration of MB@NH_2-Fe-MOF-Zn, the immune reaction time, and the number of electrodeposition cycles of AuNPs have been optimized. The pH has a great influence on the protein structure and activity. Thus, the electrochemical response of the immunosensor was measured under different pH (4.0−8.0) conditions. It can be seen from Figure S5a that the current response of the biosensor was enhanced by increasing pH values up to 7.0. Subsequently, the response signal decreased with increasing pH value. The maximum response signal was achieved at pH = 7.0, which was selected as the optimum condition.

The role of MB@NH_2-Fe-MOF-Zn is to enhance the conductivity and capture Ab_2, and its amount has an important effect on the electrochemical response. The current signal increased as the concentration was increased from 1.0 to 5.0 mg/mL, followed by a decrease when the concentration exceeded 5.0 mg/mL (Figure S5b). The 5.0 mg/mL MB@NH_2-Fe-MOF-Zn represents the efficient conductibility and the unique catalytic performance of this immunosensor. Therefore, the MB@NH_2-Fe-MOF-Zn concentration of 5.0 mg/mL was chosen as the optimal concentration.

The immune reaction time between CD44 and Ab_1 was also optimized. The results (Figure S5c) revealed that the optimal immune reaction time was preferably 60 min. Finally, the number of electrodeposition cycles of AuNPs as signal amplification was optimized (Figure S5d). The optimal peaks

https://doi.org/10.1021/acssensors.2c01215
ACS Sens. 2022, 7, 2701−2709

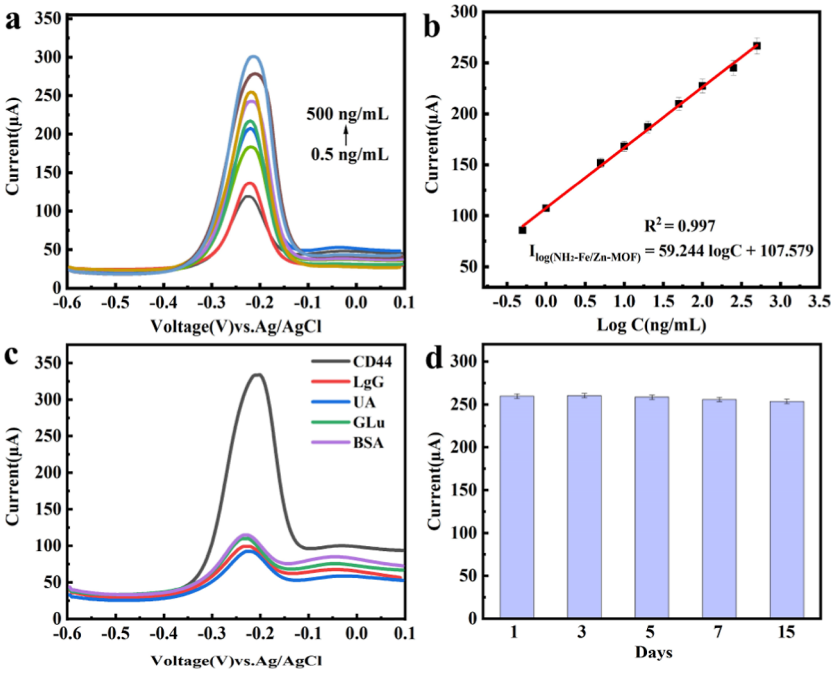

Figure 5. (a) DPV of 0.5−500 ng/mL CD44 at immunosensor in 0.1 M PBS (pH = 7.0) with a scan rate of 100 mV s^{-1}. (b) Calibration curves of immunosensor to different concentrations of CD44, error bar = RSD (n = 5). (c) Selectivity of the immunosensor for CD44 (500 ng/mL). (d) Stability of the immunosensor, error bar = RSD (n = 5).

with the highest current signals were increased for 10 cycles of AuNP electrodeposition. After 10 cycles, the optimal peaks slightly diminish. The optimal number of cycles for electrodeposition of AuNPs was selected to be 10 cycles.

Analytical Performance of the Immunosensor for CD44 and CD44$^+$ Cancer Cell Detection. In this work, the CD44 Ab_1 was immobilized on PM/AuNPs/d-V_2C/GCE. MB@NH_2-Fe-MOF-Zn/Ab_2 was used as a tracer for the detection of CD44. The analytical performance of the engineered immunosensor was investigated by measuring the DPV response current under the above optimal experimental conditions. As shown in Figure 5a, the DPV signal value of the biosensor enhanced with the increase of the concentrations of CD44. The calibration curve demonstrates a good linear relationship between current and the logarithm of CD44 concentration covering the concentration range from 0.5 to 500 ng/mL, and its linear regression equation is expressed as follows: I = 107.57 + 59.24 log C (ng/mL) (Figure 5b). The detection limit is calculated to be 1.4 pg/mL based on the signal corresponding to three times noise of the response (S/N = 3). Besides, our proposed biosensor showed comparable or better analytical performance compared with previously reported means for detecting CD44 (Table S1).

High specificity is considered as a primary characteristic for an immunosensor. Different sandwich-type immunosensors were prepared in the presence of 500 ng/mL CD44, lgG, UA, GLu, and BSA (Figure 5c). Due to the particular structure of the antibody, the immunosensor could specifically recognize the corresponding antigen. According to Figure 5c, the sandwich-type immunosensor showed good selectivity for target CD_{44} recognition. To analyze the reproducibility of the constructed sensor, five different electrodes were prepared to detect CD44 (500 ng/mL) under the same experimental conditions. The relative standard deviation (RSD) was 2.82% (Figure S6), which reveals that the immunosensor has good reproducibility along with approved accuracy of this method. Besides, the stability of the immunosensor was explored. After being stored at 4 °C for 15 days, the DPV signal gradually decreased and retained 96.4% of the initial current (Figure 5d). Therefore, the immunosensor has satisfactory properties that are beneficial for long-term storage and transport in practical applications. To investigate the accuracy of the electrochemical immunosensor for the analysis of real samples, different concentrations of CD44 standards were spiked into human serum samples. The developed biosensor was then used for the assay, and the corresponding recovery was calculated. As shown in Table S2, the recoveries of the samples were between 96.1 and 106.2%, indicating that the constructed sensor can be applied to the determination of actual samples.

Accurate identification of surface biomarker CD44 on breast cancer cells can provide important information on cancer treatment and diagnosis. Thus, the analysis platform was further employed for the identification of CD44-positive breast cancer cells. Figure S7a shows the electrochemical signals obtained in a series of MDA-MB-231 cell suspension at concentrations of 10^3 to 10^6 cells/mL. The linear regression equation of MDA-MB-231 cells is expressed as I_{pc} = 59.42 log C + 95.58, and the detection limit is calculated to be 140 cells/mL based on the signal corresponding to three times noise of the response (Figure S7b). In addition, as shown in Figure S7c,d, the electrochemical signal increased proportionally to the logarithm of the concentration of MCF-7 cells ranging from 10^3 to 10^6 cells/mL. Comprehensively, the detection of CD44 in cellular samples confirms this selective approach, providing its potential use in real samples for clinical diagnostics.

CONCLUSIONS

In conclusion, we have successfully developed a facial and sensitive sandwich-type electrochemical antifouling method

https://doi.org/10.1021/acssensors.2c01215
ACS Sens. 2022, 7, 2701−2709

based on cell membrane/V_2C MXene for CD44 detection in complex biological fluids. The sensor displayed the following key advantages: (i) construction of cell membrane coatings with excellent biocompatibility and anti-biofouling to efficiently repel non-specific proteins; (ii) assembly of V_2C-AuNPs nanocomposites to enhance the sensor performance; (iii) use of functionalized NH_2-Fe-MOF-Zn to load the signal probe MB and covalently linked antibody molecules; and (iv) detection of CD44 and $CD44^+$ cancer cells in a complex sample. This strategy for biosensor fabrication based on a simplistic and general cell membrane coating opens a promising avenue to construct other sensing systems capable of analysis in complex media. In addition, the excellent analytical platform for the detection of CD44 provides a useful tool for studying more receptor molecules on cells and efficiently assessing cellular heterogeneity.

■ ASSOCIATED CONTENT

Supporting Information

The Supporting Information is available free of charge at https://pubs.acs.org/doi/10.1021/acssensors.2c01215.

XPS spectra of d-V_2C nanosheets and NH_2-Fe-MOF-Zn; size and zeta potential of the PM; EIS response at d-V_2C/GCE and multi-layer V_2C/GCE; Effect of pH, amount of MB@NH_2-Fe-MOF-Zn, immune reaction time, and electrodeposition cycle numbers; and DPV curves of $CD44^+$ cancer cells (PDF)

■ AUTHOR INFORMATION

Corresponding Authors

Meiling Lian − *Tianjin Engineering Research Center of Civil Aviation Energy Environment and Green Development, School of Transportation Science and Engineering, Civil Aviation University of China, Tianjin 300300, P.R. China;* orcid.org/0000-0002-1656-3719; Email: mllian@cauc.edu.cn

Da Chen − *Tianjin Engineering Research Center of Civil Aviation Energy Environment and Green Development, School of Transportation Science and Engineering, Civil Aviation University of China, Tianjin 300300, P.R. China;* orcid.org/0000-0001-5135-0615; Email: dachen@tju.edu.cn

Authors

Yuqing Shi − *Tianjin Engineering Research Center of Civil Aviation Energy Environment and Green Development, School of Transportation Science and Engineering, Civil Aviation University of China, Tianjin 300300, P.R. China*

Liuxing Chen − *Tianjin Engineering Research Center of Civil Aviation Energy Environment and Green Development, School of Transportation Science and Engineering, Civil Aviation University of China, Tianjin 300300, P.R. China*

Yongji Qin − *Institute for New Energy Materials and Low-Carbon Technologies, Tianjin Key Lab for Photoelectric Materials & Devices, School of Materials Science and Engineering, Tianjin University of Technology, Tianjin 300384, P.R. China;* orcid.org/0000-0003-4900-5219

Wei Zhang − *Tianjin Engineering Research Center of Civil Aviation Energy Environment and Green Development, School of Transportation Science and Engineering, Civil Aviation University of China, Tianjin 300300, P.R. China*

Jingbo Zhao − *Tianjin Engineering Research Center of Civil Aviation Energy Environment and Green Development, School of Transportation Science and Engineering, Civil Aviation University of China, Tianjin 300300, P.R. China*

Complete contact information is available at: https://pubs.acs.org/10.1021/acssensors.2c01215

Author Contributions

The manuscript was written through contributions of all authors. All authors have given approval to the final version of the manuscript.

Notes

The authors declare no competing financial interest.

■ ACKNOWLEDGMENTS

We gratefully acknowledge the National Natural Science Foundation of China (22004130, 21973111), the Fundamental Research Funds for the Central Universities (3122021056), and the Scientific Research Project of Tianjin Education Commission (2021KJ057).

■ REFERENCES

(1) Shamsuddin, S. H.; Gibson, T. D.; Tomlinson, D. C.; McPherson, M. J.; Jayne, D. G.; Millner, P. A. Reagentless Affimer- and antibody-based impedimetric biosensors for CEA-detection using a novel non-conducting polymer. *Biosens. Bioelectron.* **2021**, *178*, 113013.

(2) Cai, G.; Yu, Z.; Ren, R.; Tang, D. Exciton−Plasmon Interaction between AuNPs/Graphene Nanohybrids and CdS Quantum Dots/TiO_2 for Photoelectrochemical Aptasensing of Prostate-Specific Antigen. *ACS Sens.* **2018**, *3*, 632−639.

(3) Li, Y.; Zeng, R.; Wang, W.; Xu, J.; Gong, H.; Li, L.; Li, M.; Tang, D. Size-Controlled Engineering Photoelectrochemical Biosensor for Human Papillomavirus-16 Based on CRISPR-Cas12a-Induced Disassembly of Z-Scheme Heterojunctions. *ACS Sens.* **2022**, *7*, 1593−1601.

(4) Jiang, C.; Wang, G. X.; Hein, R.; Liu, N. Z.; Luo, X. L.; Davis, J. J. Antifouling Strategies for Selective In Vitro and In Vivo Sensing. *Chem. Rev.* **2020**, *120*, 3852−3889.

(5) Río, J. S. d.; Henry, O. Y. F.; Jolly, P.; Ingber, D. E. An antifouling coating that enables affinity-based electrochemical biosensing in complex biological fluids. *Nat. Nanotechnol.* **2019**, *14*, 1143−1149.

(6) Russo, M. J.; Han, M. Y.; Desroches, P. E.; Manasa, C. S.; Dennaoui, J.; Quigley, A. F.; Kapsa, R. M. I.; Moulton, S. E.; Guijt, R. M.; Greene, G. W.; Silva, S. M. Antifouling Strategies for Electrochemical Biosensing: Mechanisms and Performance toward Point of Care Based Diagnostic Applications. *ACS Sens.* **2021**, *6*, 1482−1507.

(7) Feng, T. T.; Ji, W. L.; Zhang, Y.; Wu, F.; Tang, Q.; Wei, H.; Mao, L. Q.; Zhang, M. N. Zwitterionic Polydopamine Engineered Interface for In Vivo Sensing with High Biocompatibility. *Angew. Chem., Int. Ed.* **2020**, *59*, 23445−23449.

(8) Hui, N.; Sun, X.; Niu, S.; Luo, X. PEGylated Polyaniline Nanofibers: Antifouling and Conducting Biomaterial for Electrochemical DNA Sensing. *ACS Appl. Mater. Interfaces* **2017**, *9*, 2914−2923.

(9) Song, Z.; Ma, Y. H.; Chen, M.; Ambrosi, A.; Ding, C. F.; Luo, X. L. Electrochemical Biosensor with Enhanced Antifouling Capability for COVID-19 Nucleic Acid Detection in Complex Biological Media. *Anal. Chem.* **2021**, *93*, 5963−5971.

(10) Li, Y.; Han, R.; Chen, M.; Zhang, L. Y.; Wang, G. X.; Luo, X. L. Bovine Serum Albumin-Cross-Linked Polyaniline Nanowires for Ultralow Fouling and Highly Sensitive Electrochemical Protein Quantification in Human Serum Samples. *Anal. Chem.* **2021**, *93*, 4326−4333.

(11) Zhao, S. J.; Liu, N. Z.; Wang, W. Q.; Xu, Z. Y.; Wu, Y. M.; Luo, X. L. An electrochemical biosensor for alpha-fetoprotein detection in human serum based on peptides containing isomer D-Amino acids with enhanced stability and antifouling property. *Biosens. Bioelectron.* **2021**, *190*, 113466.
(12) Huang, W.; Guo, P.; Li, B.; Fu, L.; Lin, C. T.; Yu, A. M.; Lai, G. S. Enzyme-catalyzed deposition of polydopamine for amplifying the signal inhibition to a novel Prussian blue-nanocomposite and ultrasensitive electrochemical immunosensing. *J. Mater. Sci. Technol.* **2022**, *102*, 166−173.
(13) Liu, X. M.; Xiao, T. F.; Wu, F.; Shen, M. Y.; Zhang, M. N.; Yu, H. H.; Mao, L. Q. Ultrathin Cell-Membrane-Mimic Phosphorylcholine Polymer Film Coating Enables Large Improvements for In Vivo Electrochemical Detection. *Angew. Chem., Int. Ed.* **2017**, *56*, 11802−11806.
(14) Nie, D.; Dai, Z.; Li, J. L.; Yang, Y. W.; Xi, Z. Y.; Wang, J.; Zhang, W.; Qian, K.; Guo, S. Y.; Zhu, C. L.; Wang, R.; Li, Y. M.; Yu, M. R.; Zhang, X. X.; Shi, X. H.; Gan, Y. Cancer-Cell-Membrane-Coated Nanoparticles with a Yolk−Shell Structure Augment Cancer Chemotherapy. *Nano Lett.* **2020**, *20*, 936−946.
(15) Zhang, Q. Z.; Honko, A.; Zhou, J. R.; Gong, H.; Downs, S. N.; Vasquez, J. V.; Fang, R. H.; Gao, W. W.; Griffiths, A.; Zhang, L. F. Cellular Nanosponges Inhibit SARS-CoV-2 Infectivity. *Nano Lett.* **2020**, *20*, 5570−5574.
(16) Zhou, X. X.; Luo, B.; Kang, K.; Zhang, Y. J.; Jiang, P. P.; Lan, F.; Yi, Q. Y.; Wu, Y. Leukocyte-Repelling Biomimetic Immunomagnetic Nanoplatform for High-Performance Circulating Tumor Cells Isolation. *Small* **2019**, *15*, 1900558.
(17) Cheng, G.; Li, W. Q.; Ha, L.; Han, X. H.; Hao, S. J.; Wan, Y.; Wang, Z. G.; Dong, F. P.; Zou, X.; Mao, Y. W.; Zheng, S. Y. Self-Assembly of Extracellular Vesicle-like Metal−Organic Framework Nanoparticles for Protection and Intracellular Delivery of Biofunctional Proteins. *J. Am. Chem. Soc.* **2018**, *140*, 7282−7291.
(18) Meng, Q. F.; Cheng, Y. X.; Huang, Q. Q.; Zan, M. H.; Xie, W.; Sun, Y.; Li, R.; Wei, X. Y.; Guo, S. S.; Zhao, X. Z.; Rao, L.; Liu, W. Biomimetic Immunomagnetic Nanoparticles with Minimal Nonspecific Biomolecule Adsorption for Enhanced Isolation of Circulating Tumor Cells. *ACS Appl. Mater. Interfaces* **2019**, *11*, 28732−28739.
(19) Kumar, S.; Han, J. A.; Michael, I. J.; Ki, D.; Sunkara, V.; Park, J.; Gautam, S.; Ha, H. K.; Zhang, L. F.; Cho, Y. K. Human platelet membrane functionalized microchips with plasmonic codes for cancer detection. *Adv. Funct. Mater.* **2019**, *29*, 1902669.
(20) Dong, Z. Y.; Ke, X.; Tang, S. X.; Wu, S.; Wu, W.; Chen, X. Y.; Yang, J. J.; Xie, J.; Luo, J.; Li, J. S. A Stable Cell Membrane-Based Coating with Antibiofouling and Macrophage Immunoregulatory Properties for Implants at the Macroscopic Level. *Chem. Mater.* **2021**, *33*, 7994−8006.
(21) Cao, Y.; Yu, X. M.; Han, B.; Dong, L. J.; Xu, J. J.; Dai, Y. H.; Li, G. X.; Zhao, J. In Situ Programmable DNA Circuit-Promoted Electrochemical Characterization of Stemlike Phenotype in Breast Cancer. *J. Am. Chem. Soc.* **2021**, *143*, 16078−16086.
(22) Soomro, R. A.; Jawaid, S.; Kalawar, N. H.; Tunesi, M.; Karakuş, S.; Kilislioğlu, A.; Willander, M. In-situ engineered MXene-TiO2/BiVO4 hybrid as an efficient photoelectrochemical platform for sensitive detection of soluble CD44 proteins. *Biosens. Bioelectron.* **2020**, *166*, 112439.
(23) Zhang, R.; Rejeeth, C.; Xu, W.; Zhu, C. Y.; Liu, X. Y.; Wan, J. J.; Jiang, M. W.; Qian, K. Label-Free Electrochemical Sensor for CD44 by Ligand-Protein Interaction. *Anal. Chem.* **2019**, *91*, 7078−7085.
(24) Qiu, Y. Y.; Zhou, B.; Yang, X. J.; Long, D. P.; Hao, Y.; Yang, P. H. Novel Single-Cell Analysis Platform Based on a Solid-State Zinc-Coadsorbed Carbon Quantum Dots Electrochemiluminescence Probe for the Evaluation of CD44 Expression on Breast Cancer Cells. *ACS Appl. Mater. Interfaces* **2017**, *9*, 16848−16856.
(25) Zhao, J.; Tang, Y. Y.; Cao, Y.; Chen, T. S.; Chen, X. X.; Mao, X. X.; Yin, Y. M.; Chen, G. F. Amplified electrochemical detection of surface biomarker in breast cancer stem cell using self-assembled supramolecular nanocomposites. *Electrochim. Acta* **2018**, *283*, 1072−1078.
(26) Kumar, P.; Singh, S.; Hashmi, S. A. R.; Kim, K. K. MXenes: Emerging 2D materials for hydrogen storage. *Nano Energy* **2021**, *85*, 105989.
(27) Ding, L.; Wei, Y.; Wang, Y.; Chen, H.; CaroJ, G.; Wang, H. A Two-Dimensional Lamellar Membrane: MXene Nanosheet Stacks. *Angew. Chem., Int. Ed.* **2017**, *56*, 1825.
(28) Pei, Y. Y.; Zhang, X. L.; Hui, Z. Y.; Zhou, J. Y.; Huang, X.; Sun, G. Z.; Huang, W. Ti_3C_2TX MXene for Sensing Applications: Recent Progress, Design Principles, and Future Perspectives. *ACS Nano* **2021**, *15*, 3996−4017.
(29) Cai, G.; Yu, Z.; Tong, P.; Tang, D. Ti_3C_2 MXene quantum dot-encapsulated liposomes for photothermal immunoassays using a portable near-infrared imaging camera on a smartphone. *Nanoscale* **2019**, *11*, 15659.
(30) Chen, J.; Tong, P.; Huang, L.; Yu, Z.; Tang, D. Ti_3C_2 MXene nanosheet-based capacitance immunoassay with tyramine-enzyme repeats to detect prostate-specific antigen on interdigitated microcomb electrode. *Electrochim. Acta* **2019**, *319*, 375−381.
(31) Zeng, R.; Wang, W.; Chen, M.; Wan, Q.; Wang, C.; Knopp, D.; Tang, D. CRISPR-Cas12a-driven MXene-PEDOT:PSS piezoresistive wireless biosensor. *Nano Energy* **2021**, *82*, 105711.
(32) Ghasali, E.; Orooji, Y.; Azarniya, A.; Alizadeh, M.; Kazem-zad, M.; TouradjEbadzadeh, T. Production of V_2C MXene using a repetitive pattern of V_2AlC MAX phase through microwave heating of Al-V_2O_5-C system. *Appl. Surf. Sci.* **2021**, *542*, 148538.
(33) Shan, Q. S.; Mu, X. P.; Alhabeb, M.; Shuck, C. E.; Pang, D.; Zhao, X.; Chu, X. F.; Wei, Y. J.; Du, F.; Chen, G.; Gogotsi, Y.; Gao, Y.; Dall'Agnese, Y. Two-dimensional vanadium carbide (V_2C) MXene as electrode for supercapacitors with aqueous electrolytes. *Electrochem. Commun.* **2018**, *96*, 103−107.
(34) Liu, H. Z.; Lu, C. L.; Wang, Z. C.; Xu, L.; Huang, X. T.; Wang, X. H.; Ning, H.; Lan, Z. Q.; Guo, J. Combinations of V_2C and Ti_3C_2 MXenes for Boosting the Hydrogen Storage Performances of MgH_2. *ACS Appl. Mater. Interfaces* **2021**, *13*, 13235−13247.
(35) Liu, F. F.; Liu, Y. C.; Zhao, X. D.; Liu, K. Y.; Yin, H. Q.; Fan, L. Z. Prelithiated V_2C MXene: A High-Performance Electrode for Hybrid Magnesium/Lithium-Ion Batteries by Ion Cointercalation. *Small* **2020**, *16*, 1906076.
(36) Han, J.; Zhang, M. F.; Chen, G. J.; Zhang, Y. Q.; Wei, Q.; Zhuo, Y.; Xie, G.; Yuan, R.; Chen, S. P. Ferrocene covalently confined in porous MOF as signal tag for highly sensitive electrochemical immunoassay of amyloid-β. *J. Mater. Chem. B* **2017**, *5*, 8330−8336.
(37) Zheng, X. X.; Shen, L. J.; Chen, X. P.; Zheng, Z. H.; Au, C. T.; Jiang, L. L. Amino-Modified Fe-Terephthalate Metal−Organic Framework as an Efficient Catalyst for the Selective Oxidation of H_2S. *Inorg. Chem.* **2018**, *57*, 10081−10089.
(38) Rao, L.; Bu, L.-L.; Meng, Q.-M.; Cai, B.; Deng, W.-W.; Li, A.; Li, K.; Guo, S.-S.; Zhang, W.-F.; Liu, W.; Sun, Z.-J.; Zhao, X. Z. Antitumor platelet-mimicking magnetic nanoparticles. *Adv. Funct. Mater.* **2017**, *27*, 1604774.

https://doi.org/10.1021/acssensors.2c01215
ACS Sens. 2022, 7, 2701−2709